Nematic, chiral, and topological superconductivity in twisted transition metal dichalcogenides

Constantin Schrade[1] and Liang Fu[2]
[1]*Hearne Institute of Theoretical Physics, Department of Physics and Astronomy, Louisiana State University, Baton Rouge, Louisiana 70803, USA*
[2]*Department of Physics, Massachusetts Institute of Technology, 77 Massachusetts Avenue, Cambridge, Massachusetts 02139, USA*

(Received 23 September 2021; revised 5 June 2024; accepted 11 June 2024; published 17 July 2024; corrected 29 July 2024)

We introduce and study a realistic model for superconductivity in twisted bilayer WSe_2, where electron pairing arises from spin-valley fluctuations in the weak-coupling regime. Our model comprises both the full continuum model moiré band structure and a short-ranged repulsive interaction. By calculating the spin-valley susceptibility, we identify a significant enhancement of the spin-valley fluctuations near half filling of the topmost moiré band. We then analyze the dominant Kohn-Luttinger pairing instabilities due to these spin-valley fluctuations and show that the leading instability corresponds to a two-component order parameter, which can give rise to nematic, chiral, and topological superconductivity. As our findings are asymptotically exact for small interaction strengths, they provide a viable starting point for future studies of superconductivity in twisted transition metal dichalcogenide bilayers.

DOI: 10.1103/PhysRevB.110.035143

I. INTRODUCTION

Two-dimensional transition metal dichalcogenides (TMDs) have in recent years emerged as a promising material platform for realizing a plethora of new electronic phases [1]. Prominent examples of these electronic phases in monolayer TMDs include the quantum spin Hall effect [2–5], arising due to the strongly spin-orbit coupled band structure, and Ising superconductivity [6–9], which is realized as a result of the substantial effective electron mass that enhances the importance of interaction effects.

Beyond the TMD monolayers, another research frontier that is currently evolving at a rapid pace is moiré lattices realized with multilayer TMDs [10–18]. In these systems, a lattice mismatch or a rotational misalignment generates an effective superlattice that can be utilized for simulating strongly correlated electron states [19–28]. For example, in WSe_2/WS_2 heterobilayers, experiments have identified Mott insulators [10,11], Wigner crystals [10], and stripe-ordered states [12]. Moreover, in twisted WSe_2 ($tWSe_2$) homobilayers, experiments have found evidence for quantum criticality [13] and correlated insulating states [14]. Notably, the discovered correlated insulators in $tWSe_2$ appeared at half filling for a broad twist angle range, $\theta \sim 4^\circ$–5.1°, for which the bandwidth is likely comparable to the interaction strength. This weak- to intermediate-coupling scenario is further supported by a resistivity enhancement upon tuning a van Hove singularity to half filling via an external displacement field. Both features highlight the *importance of band-structure effects* for understanding correlated electron states in $tWSe_2$ [29].

In addition to the discovery of correlated insulators, an experiment on $tWSe_2$ also found a "zero-resistance state" when doping away from half filling at $\theta \sim 5.1^\circ$ [14]. The appearance of this zero-resistance state indicates that, similar to graphene-based superlattices [30–36], $tWSe_2$ can also host superconductivity. However, it is so far unclear what properties of the band structure can effect the candidate superconducting state in $tWSe_2$. Moreover, it is also an open question on what constitutes the pairing mechanism and pairing symmetry.

Here, we address these questions by introducing a model for superconductivity in $tWSe_2$, where electron pairing arises from spin-valley fluctuations. Our model comprises both the moiré band structure of $tWSe_2$ and a short-ranged repulsive interaction. Near half filling of the topmost moiré band, we demonstrate that the Fermi surfaces of the $\pm K$ valleys exhibit a strong nesting feature. This nesting maps the occupied states of one valley onto the other valley's unoccupied states, leading to strong spin-valley fluctuations especially near the insulating state [29]. We show that, interestingly, electron pairing mediated by such enhanced spin-valley fluctuations can give rise to nematic, chiral, and topological superconductivity. Our findings are asymptotically exact in the weak-coupling limit [37] and provide a starting point for studies of superconductivity in TMD systems.

II. MODEL

A. Continuum model Hamiltonian

We consider two layers of WSe_2 that are initially aligned in the AA-stacking configuration and, subsequently, rotated by a small twist angle θ [see Fig. 1(a)]. In this situation, the $\pm K$ valleys of the layers have comparable energy so that interlayer tunneling becomes effective, which leads to a layer-hybridized moiré band structure. For the discussion of this moiré band structure, we focus separately on the spin-up (spin-down) valence bands of the $+K$ ($-K$) valleys. This approach is justified by the substantial valley-dependent spin splitting in the valence bands and the effective decoupling of the valleys due to their large momentum space separation. The Hamiltonian

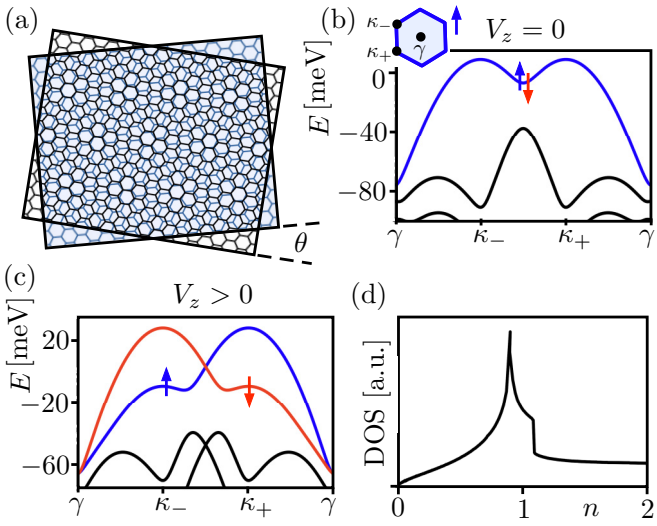

FIG. 1. (a) WSe_2 layers at twist angle θ forming a triangular moiré lattice. (b) The band structure E along high-symmetry lines for $(\theta, V_z, V, \psi, w) = (5.1^\circ, 0\text{ meV}, 9\text{ meV}, 128^\circ, 18\text{ meV})$. The inset shows the moiré Brillouin zone at the $+K$ valleys. (c) Same as (b) but for $V_z = 42$ meV. The spin-up (blue) and spin-down (red) bands at the $\pm K$ valleys are split by the finite displacement field. (d) DOS with a maximum near $n_{\max} \approx 0.9$.

for the continuum model moiré bands of spin-up electrons at the $+K$ valleys then reads [20]

$$H_\uparrow = \int \mathrm{d}\boldsymbol{r}\, \Psi_\uparrow^\dagger(\boldsymbol{r}) \begin{pmatrix} h^t_{\boldsymbol{k}\uparrow}(\boldsymbol{r}) & \Delta_T(\boldsymbol{r}) \\ \Delta_T^\dagger(\boldsymbol{r}) & h^b_{\boldsymbol{k}\uparrow}(\boldsymbol{r}) \end{pmatrix} \Psi_\uparrow(\boldsymbol{r}), \tag{1}$$

where $\Psi_\uparrow(\boldsymbol{r}) = [c^t_\uparrow(\boldsymbol{r}), c^b_\uparrow(\boldsymbol{r})]^T$ is an electron spinor with components corresponding to the top/bottom (t/b) layer. The Hamiltonian for spin-down electrons at the $-K$ valleys is obtained from $H_\uparrow$ via a time-reversal operation.

First, we discuss the diagonal components of $H_\uparrow$, which represent the individual layers. They are given by

$$h^{t/b}_{\boldsymbol{k}\uparrow}(\boldsymbol{r}) = -\frac{\hbar^2(\boldsymbol{k}-\boldsymbol{\kappa}_\pm)^2}{2m^*} \pm \frac{V_z}{2} + \sum_{j=1,3,5} 2V\cos(\boldsymbol{b}_j\cdot\boldsymbol{r} \pm \psi). \tag{2}$$

Here, the first term describes the kinetic energy with effective mass $m^* = 0.43 m_0$ (m_0 is the bare electron mass) and momentum shifts $\boldsymbol{\kappa}_\pm = [4\pi|\theta|/(3a_0)](-\sqrt{3}/2, \mp 1/2)$ ($a_0 = 3.317$ Å is the monolayer lattice constant), that account for for the layer rotation in momentum space. The second term corresponds to a layer potential difference V_z due to an out-of-plane displacement field. The third term models the moiré potential with amplitude V, phase offset ψ, and reciprocal lattice vectors $\boldsymbol{b}_j = C_3^{j-1}(4\pi|\theta|/\sqrt{3}a_0, 0)$ (C_3 is a $2\pi/3$ rotation).

Besides the individual layer terms, $H_\uparrow$ also includes off-diagonal terms for interlayer coupling. They read

$$\Delta_T(\boldsymbol{r}) = w(1 + e^{-i\boldsymbol{b}_2\cdot\boldsymbol{r}} + e^{-i\boldsymbol{b}_3\cdot\boldsymbol{r}}), \tag{3}$$

where w corresponds to the interlayer coupling strength.

Having defined the continuum model Hamiltonian, we now proceed by analyzing its spatial symmetries. We find that the continuum model exhibits a threefold rotation symmetry given by $U^\dagger_{C_3}(\boldsymbol{r})H_{C_3(\boldsymbol{k})\uparrow}(C_3(\boldsymbol{r}))U_{C_3}(\boldsymbol{r}) = H_{\boldsymbol{k}\uparrow}(\boldsymbol{r})$ with the Hamiltonian density $H_{\boldsymbol{k}\uparrow}(\boldsymbol{r})$, $U_{C_3}(\boldsymbol{r}) = e^{i(1+\tau_z/2)\boldsymbol{b}_2\cdot\boldsymbol{r}_2}e^{i\boldsymbol{b}_3\cdot\boldsymbol{r}}$, and a layer-space Pauli matrix τ_z. Besides the rotation symmetry, which is also a microscopic symmetry of the moiré lattice, the continuum model exhibits an emergent mirror symmetry along $y = 0$ given by $H_{M_x(\boldsymbol{k})\uparrow}[M_x(\boldsymbol{r})] = H_{\boldsymbol{k}\downarrow}(\boldsymbol{r})$. Interestingly, this mirror symmetry flips the two valleys.

B. Moiré band structure

As a final step, we plot the moiré bands along the high-symmetry lines of the Brillouin zone for $(\theta, V, \psi, w) = (5.1^\circ, 9\text{ meV}, 128^\circ, 18\text{ meV})$ [26] with $V_z = 0$ meV and $V_z = 42$ meV [see Figs. 1(b) and 1(c)]. We find that finite displacement field induces an approximate saddle point in the topmost moiré bands $\xi_{\uparrow/\downarrow}(\boldsymbol{k})$ at $\boldsymbol{\kappa}_\pm$. At these points, the Fermi velocity is greatly reduced, which leads to an enhancement of the density of states (DOS) for a filling of $n \approx 0.9$ electrons per moiré unit cell [see Fig. 1(d)]. The emergence of an enhanced DOS near $n \approx 1$ is in accordance with experiments [14] and signals that correlation effects due to spin-valley fluctuations may be amplified. In our further analysis, we will fix the above choice for (θ, V, ψ, w) that we obtained from density functional calculations [26] and the field value $V_z = 42$ meV.

III. SPIN-VALLEY FLUCTUATIONS

We now discuss the ordering instabilities that arise from the spin-valley fluctuations. To identify the spin-valley fluctuations with dominant modulation vectors, we will analyze the maxima of the spin-valley susceptibility,

$$\chi_{\alpha\beta}(\boldsymbol{q}, \omega) = -\frac{1}{\beta N}\sum_{\boldsymbol{k}} \mathrm{Tr}[\sigma_\alpha G(\boldsymbol{k}, i\omega)\sigma_\beta G(\boldsymbol{k}+\boldsymbol{q}, i\omega)]. \tag{4}$$

In this definition, $\sigma_{\alpha,\beta} \in \{\sigma_z, \sigma_\pm = (\sigma_x \pm i\sigma_y)/2\}$ are spin/valley-space Pauli matrices, "Tr" denotes the trace over the spin/valley indices, β is the inverse temperature, and N is the number of superlattice unit cells. Furthermore, the noninteracting Green's function is given by

$$G_{s_1 s_2}(\boldsymbol{k}, i\omega) = \delta_{s_1 s_2}\big[i\omega - \xi_{s_1}(\boldsymbol{k}) + \mu\big]^{-1}. \tag{5}$$

Here, $\xi_s(\boldsymbol{k})$ are the dispersions for the topmost moiré band of the $\pm K$ valleys with $\xi_\downarrow(\boldsymbol{k}) = \xi_\uparrow(-\boldsymbol{k})$ due to time-reversal symmetry, μ is the chemical potential, and ω corresponds to a fermionic Matsubara frequency.

Having defined the spin-valley susceptibility, we will now investigate its static longitudinal and transversal components, $\chi_{zz}(\boldsymbol{q}) = \chi_{zz}(\boldsymbol{q}, 0)$ and $\chi_{+-}(\boldsymbol{q}) = \chi_{+-}(\boldsymbol{q}, 0)$. In our system, $\xi_{zz}(\boldsymbol{q})$ and $\xi_{+-}(\boldsymbol{q})$ are different because of the broken SU(2) valley rotation symmetry.

First, we focus on the filling of $n \approx 1$ electron per moiré unit cell because it is the experimentally most relevant case. In this situation, the Fermi surfaces have the shape of triangles centered around the γ point of the Brillouin zone as shown in Fig. 2(a). As shown in Fig. 2(b), we numerically find that $\chi_{+-}(\boldsymbol{q})$ is enhanced near $\boldsymbol{q} \approx \boldsymbol{Q}_j$ with $\boldsymbol{Q}_j = C_3^{j-1}\boldsymbol{\kappa}_+$, indicating an instability towards an intervalley excitonic insulator

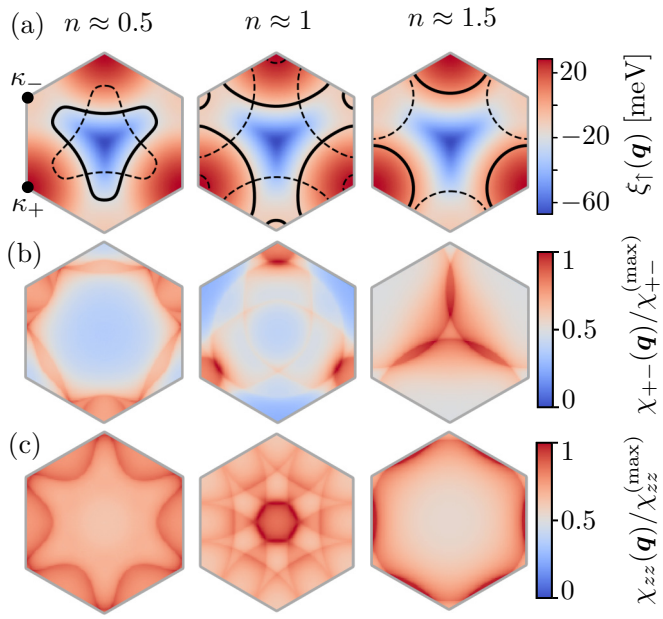

FIG. 2. (a) Dispersion $\xi_\uparrow(\boldsymbol{q})$ of the topmost band at the $+K$ valleys. The $+K$ ($-K$) valley Fermi surfaces are shown with solid (dashed) black lines. (b) Transversal spin-valley susceptibility $\chi_{+-}(\boldsymbol{q})$ at $1/\beta = 100$ meV. (c) Longitudinal spin-valley susceptibility $\chi_{zz}(\boldsymbol{q})$ at $1/\beta = 100$ meV.

that pairs electrons and holes of opposite valleys [29]. However, due to the broken SU(2) valley rotation symmetry, the same features are *not* present in the longitudinal valley susceptibility. Instead, as shown in Fig. 2(c), $\chi_{zz}(\boldsymbol{q})$ is enhanced near $\boldsymbol{q} \approx \boldsymbol{0}$, suggesting that the excitonic instability competes with a spin/valley-polarized state [26].

We now compare these results with the situation away from $n \approx 1$. For fillings $n \lesssim 0.9$, the Fermi surfaces shrink to smaller triangles and the dominant modulation vectors in the spin-valley susceptibility are modified. For example, at $n \approx 0.5$, $\chi_{+-}(\boldsymbol{q})$ is enhanced near $\boldsymbol{q} \approx \boldsymbol{Q}'_j$ with $\boldsymbol{Q}'_j = C_3^{j-1}\boldsymbol{\kappa}_-$, while $\chi_{zz}(\boldsymbol{q})$ shows maxima near the Brillouin zone boundaries. For $n > 1$, the Fermi surfaces are center at the Brillouin zone corners. At $n \approx 1.5$, $\chi_{+-}(\boldsymbol{q})$ is enhanced near $\boldsymbol{q} \approx \boldsymbol{0}$, while $\chi_{zz}(\boldsymbol{q})$ is again enhanced near the Brillouin zone edges.

IV. SUPERCONDUCTIVITY

A. Kohn-Luttinger mechanism

We will now demonstrate that spin-valley fluctuations can mediate superconductivity by a Kohn-Luttinger mechanism that realizes Cooper pairing from a nominally repulsive interaction term in the weak-coupling regime [37–40].

Before discussing the details of our approach, we highlight that the Kohn-Luttinger mechanism has also been valuable for understanding unconventional superconductivity in the intermediate-coupling regime and has already been applied to graphene systems [41–45]. For $tWSe_2$, band-structure effects remain critical for understanding correlated states in these samples. In particular, by tuning the van Hove singularity in the moiré band structure close to half filling, a significant increase in the longitudinal resistance peak was noted, which indicates the emergence of the correlated insulator state [14]. Therefore, we expect that the Kohn-Luttinger mechanism can offer qualitative insights into the realized superconducting pairing symmetry.

To start, we introduce the Hubbard Hamiltonian,

$$H = \sum_{\boldsymbol{k}s} \xi_s(\boldsymbol{k}) c^\dagger_{\boldsymbol{k}s} c_{\boldsymbol{k}s} + \frac{U}{N} \sum_{\substack{\boldsymbol{k},\boldsymbol{p},\boldsymbol{q} \\ s,s'}} c^\dagger_{\boldsymbol{q}s} c^\dagger_{\boldsymbol{p}+\boldsymbol{k}-\boldsymbol{q}s'} c_{\boldsymbol{p}s'} c_{\boldsymbol{k}s}, \tag{6}$$

where the quadratic part comprises the dispersion $\xi_s(\boldsymbol{k})$ of the topmost moiré band of the continuum model and $c_{\boldsymbol{k}s}$ is the electron annihilation operator with momentum $\boldsymbol{k}$ and spin s. In particular, as we omit multiband effects, there is an emergent mirror symmetry M_y along $x = 0$ with $\xi_s(M_y\boldsymbol{k}) = \xi_s(\boldsymbol{k})$. The interaction term in the Hamiltonian is taken as a local (compared to moiré scale) repulsive interaction with a strength $U > 0$.

Next, we compute the Cooper channel interaction vertex, which describes the scattering of electrons with spin polarization s and s' from the Fermi-surface momenta $(\hat{\boldsymbol{k}}', -\hat{\boldsymbol{k}}')$ to $(\hat{\boldsymbol{k}}, -\hat{\boldsymbol{k}})$. In general, the interaction vertex comprises a contribution from opposite-spin and equal-spin scattering. However, the equal-spin scattering leads to pairing with a "$\boldsymbol{d}$ vector" pointed orthogonal to the spin polarization [46]. Such an equal-spin pairing exhibits a suppressed critical temperature [47,48] and, hence, our focus will be on opposite-spin scattering. To second order in U, we find that the interaction vertex [49],

$$\Gamma(\hat{\boldsymbol{k}}, \hat{\boldsymbol{k}}') = U + U^2 \chi_{+-}(\hat{\boldsymbol{k}} + \hat{\boldsymbol{k}}'). \tag{7}$$

Notably, this result is different for TMD monolayers, where a parabolic dispersion induces a momentum dependence only at order U^3 [50].

Next, we perform a mean-field decoupling of the effective pairing interaction and compute the superconducting order parameter from the self-consistency equation [49],

$$\int_{\mathrm{FS}_\uparrow} \frac{d\hat{\boldsymbol{k}}'}{v_\uparrow(\hat{\boldsymbol{k}}')} \Gamma(\hat{\boldsymbol{k}}, \hat{\boldsymbol{k}}') \Delta(\hat{\boldsymbol{k}}') = \lambda \Delta(\hat{\boldsymbol{k}}), \tag{8}$$

Here, $v_\uparrow(\boldsymbol{k}) = ||\partial\xi_\uparrow(\boldsymbol{k})/\partial\boldsymbol{k}||$ is the Fermi velocity and $\Delta(\hat{\boldsymbol{k}})$ is the superconducting order parameter along the $+K$ valley Fermi surface, $\xi_\uparrow(\boldsymbol{k}) = \mu$. The order parameters at the $-K$ Fermi surface, $\xi_\downarrow(\boldsymbol{k}) = \mu$, is $\Delta'(\hat{\boldsymbol{k}}) = -\Delta(-\hat{\boldsymbol{k}})$. Three remarks about Eq. (8) are in order:

(1) The negative eigenvalues $\lambda < 0$ correspond to sectors with an attractive interaction in the Cooper channel and grow in magnitude under renormalization. In particular, the most negative eigenvalue $\lambda^{(0)}$ is most relevant in the renormalization group sense, triggering the leading superconducting instability at $T_c \propto \exp(-1/|\lambda^{(0)}|)$ [37].

(2) The eigenvectors $\Delta(\boldsymbol{k})$ correspond to form factors of the superconducting order parameters and transform as irreducible representations $\{A_1, A_2, E\}$ of the point group C_{3v} that is generated by C_3 and M_y. In particular, since C_{3v} has no inversion center, singlet and triplet pairings mix in $tWSe_2$ [50,51].

(3) In the weak-coupling limit, the term $\propto U$ in $\Gamma(\hat{\boldsymbol{k}}, \hat{\boldsymbol{k}}')$ is parametrically larger than the term $\propto U^2$. For an attractive

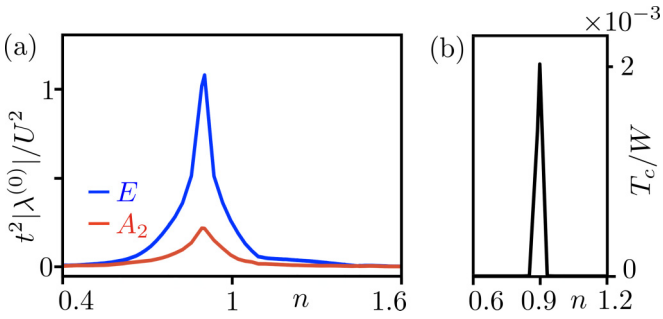

FIG. 3. (a) Pairing strength given by the most negative eigenvalue $\lambda^{(0)}$ of the self-consistency equation as a function of filling n with $t = \hbar^2\theta^2/2m^*a_0^2$. For fillings $1.4 \lesssim n \lesssim 1.45$, the most negative eigenvalue is in the $1d$ A_2 representation of the C_{3v} point group. At all other fillings, the most negative eigenvalue is in the $2d$ E representation. (b) Critical temperature normalized by the bandwidth W for $(U/t)^2 = 0.15$, showing a pronounced enhancement around $n \approx n_{\max} = 0.9$. Taking a bandwidth $W \approx 80$ meV [see Fig. 1(a)], we have $T_c \approx 1.85$ K.

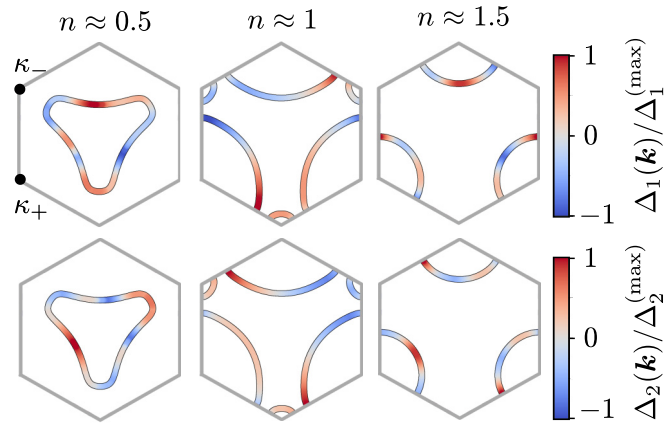

FIG. 4. Linear independent gap functions of the leading superconducting state in the E representation.

interaction in the Cooper channel, the eigenvectors $\Delta(\boldsymbol{k})$ thus must be annihilated by the leading term $\propto U$ exactly in the expression for the interaction vertex of Eq. (7) [37,52]. Or, explained differently, the eigenvectors $\Delta(\boldsymbol{k})$ need to be in the null space of the matrix representation of the first-order term $\propto U$ in Eq. (7). In particular, the s-wave pairing cannot be annihilated by the first-order term and, thus, cannot be realized. Furthermore, the absence of inversion symmetry in our system results in a mixture of singlet and triplet pairing channels. Consequently, the suppression of s-wave pairing extends to other channels within the A_1 representation [50]. Hence, the pairing needs to arise from the remaining representations, which are the $1d$ A_2 representation or the $2d$ E representation.

B. Superconducting pairings

To determine the leading eigenvalue $\lambda^{(0)}$ and the representation of the associated superconducting order parameter, we solve Eq. (8) numerically for a broad range of fillings $n \in [0.4, 1.6]$. As shown in Figs. 3 and 4, we find for $1.4 \lesssim n \lesssim 1.45$ that $\lambda^{(0)}$ is in the A_2 representation with a single-component order parameter $\Delta(\boldsymbol{k}) \propto \Delta_1(\boldsymbol{k})$. In contrast, for all other n, we find that $\lambda^{(0)}$ is in the E representation with a two-component order parameter, $\Delta(\boldsymbol{k}) = \eta_1\Delta_1(\boldsymbol{k}) + \eta_2\Delta_2(\boldsymbol{k})$. Notably, we also observe that the magnitude of $\lambda^{(0)}$, which we associate with the pairing strength, is greatly enhanced for $n \approx 0.9$. This enhanced pairing strength leads to a significant enhancement in the critical temperature T_c and suggest a pronounced tendency towards superconductivity at $n = 0.9$.

C. Ginzburg-Landau analysis

Lastly, we want to identify the superconducting state $\boldsymbol{\eta} = (\eta_1, \eta_2)$ realized in the E representation of our model. For that purpose, we write down the (C_{3v}-symmetric) Ginzburg-Landau free energy for our system,

$$F_{\rm GL} = a(T - T_c)\,\boldsymbol{\eta}\cdot\boldsymbol{\eta}^* + b_1(\boldsymbol{\eta}\cdot\boldsymbol{\eta}^*)^2 + b_2|\boldsymbol{\eta}\cdot\boldsymbol{\eta}|^2 + \cdots, \tag{9}$$

where $a > 0$ induces the superconducting phase if $T < T_c$ and $b_1 > 0$ ensures thermodynamic stability. The sign of b_2 fixes the form of the superconducting state: If $b_2 < 0$, $F_{\rm GL}$ is minimized by the *nematic state* with $\boldsymbol{\eta} = (\cos\varphi, \sin\varphi)$ and $\varphi \in [0, 2\pi)$. The latter spontaneously breaks the threefold rotation symmetry of the lattice but preserves time-reversal symmetry. If $b_2 > 0$, $F_{\rm GL}$ is minimized by the *chiral state* with $\boldsymbol{\eta} = (1, \pm i)$. The chiral state breaks time-reversal symmetry spontaneously and is characterized by chiral Majorana edge states at its boundaries.

Considering the possibility of both a chiral state or a nematic state in $tWSe_2$, an interesting question is how these possible pairing states could be detected in possible future experiments. For example, an experimental signature of the Majorana edge modes in the chiral state is a quantized thermal Hall conductivity. Another possibility is to use the polar Kerr effect or magnetic circular dichroism to detect the time-reversal symmetry breaking of the superconducting order parameter in the chiral state. The nematic state, on the other hand, could be distinguished by anisotropies in the upper critical field and optical responses [12,53,54].

V. DISCUSSION AND CONCLUSION

Having identified the pairing symmetry for a superconducting state in $tWSe_2$, it is now instructive to compare our theoretical considerations to the experimental results of Wang *et al.* [14]. As already discussed in Introduction, this experiment reported the emergence of a putative superconducting state in $tWSe_2$ upon doping away from a correlated insulator state at half filling. In the experiment, two features pointed towards the possible emergence of superconductivity: (1) a significant reduction in resistance below approximately 3 K at a twist angle of 5.1°, near half filling, and under the influence of a displacement field, and (2) a flattening of the current-voltage curve below about 2 K under the same conditions. It should be noted that the zero-resistance state observed in Ref. [14] "was unstable to repeated thermal cycling." Further experimental study is needed to establish reproducible superconductivity in $tWSe_2$.

In our theory work, we introduced a realistic model for superconductivity in $tWSe_2$ based on spin-valley fluctuations.

We have shown that the enhancement of spin-valley fluctuations around half filling can provide a mechanism for Cooper pairing and predicted an unconventional, two-component order parameter for superconductivity in $tWSe_2$, realizing either a chiral topological superconductor or a time-reversal invariant nematic superconductor. In future studies, it will be interesting to explore experimental signatures of the predicted two-component order parameter.

Note added. Recently, we became aware of two studies that reported the observation of unconventional superconductivity in $tWSe_2$ [55,56]. In particular, Ref. [56] suggests that the observed superconductivity in $tWSe_2$ at 5 degree twist angle may be mediated by spin-fluctuations, consistent with our theory.

ACKNOWLEDGMENTS

This work was supported by a Simons Investigator Award from the Simons Foundation. L.F. was supported in part by the Air Force Office of Scientific Research (AFOSR) under Award No. FA9550-22-1-0432.

[1] S. Manzeli, D. Ovchinnikov, D. Pasquier, O. V. Yazyev, and A. Kis, Nat. Rev. Mater. **2**, 17033 (2017).
[2] X. Qian, J. Liu, L. Fu, and J. Li, Science **346**, 1344 (2014).
[3] S. Tang, C. Zhang, D. Wong, Z. Pedramrazi, H.-Z. Tsai, C. Jia, B. Moritz, M. Claassen, H. Ryu, S. Kahn, J. Jiang, H. Yan, M. Hashimoto, D. Lu, R. G. Moore, C.-C. Hwang, C. Hwang, Z. Hussain, Y. Chen, M. M. Ugeda *et al.*, Nat. Phys. **13**, 683 (2017).
[4] S. Wu, V. Fatemi, Q. D. Gibson, K. Watanabe, T. Taniguchi, R. J. Cava, and P. Jarillo-Herrero, Science **359**, 76 (2018).
[5] Y. Shi, J. Kahn, B. Niu, Z. Fei, B. Sun, X. Cai, B. A. Francisco, D. Wu, Z.-X. Shen, X. Xu, D. H. Cobden, and Y.-T. Cui, Sci. Adv. **5**, eaat8799 (2019).
[6] J. M. Lu, O. Zeliuk, I. Leermakers, N. F. Q. Yuan, U. Zeitler, K. T. Law, and J. T. Ye, Science **350**, 1353 (2015).
[7] X. Xi, Z. Wang, W. Zhao, J.-H. Park, K. T. Law, H. Berger, L. Forró, J. Shan, and K. F. Mak, Nat. Phys. **12**, 139 (2016).
[8] E. Sohn, X. Xi, W.-Y. He, S. Jiang, Z. Wang, K. Kang, J.-H. Park, H. Berger, L. Forró, K. T. Law, J. Shan, and K. F. Mak, Nat. Mater. **17**, 504 (2018).
[9] S. C. de la Barrera, M. R. Sinko, D. P. Gopalan, N. Sivadas, K. L. Seyler, K. Watanabe, T. Taniguchi, A. W. Tsen, X. Xu, D. Xiao, and B. Hunt, Nat. Commun. **9**, 1427 (2018).
[10] E. C. Regan, D. Wang, C. Jin, M. I. B. Utama, B. Gao, X. Wei, S. Zhao, W. Zhao, K. Yumigeta, M. Blei, J. Carlstroem, K. Watanabe, T. Taniguchi, S. Tongay, M. Crommie, A. Zettl, and F. Wang, Nature (London) **579**, 359 (2020).
[11] Y. Tang, L. Li, T. Li, Y. Xu, S. Liu, K. Barmak, K. Watanabe, T. Taniguchi, A. H. MacDonald, J. Shan, and K. F. Mak, Nature (London) **579**, 353 (2020).
[12] C. Jin, Z. Tao, T. Li, Y. Xu, Y. Tang, J. Zhu, S. Liu, K. Watanabe, T. Taniguchi, J. C. Hone, L. Fu, J. Shan, and K. F. Mak, Nat. Mater. **20**, 940 (2021).
[13] A. Ghiotto, E.-M. Shih, G. S. S. G. Pereira, D. A. Rhodes, B. Kim, J. Zang, A. J. Millis, K. Watanabe, T. Taniguchi, J. C. Hone, L. Wang, C. R. Dean, and A. N. Pasupathy, Nature (London) **597**, 345 (2021).
[14] L. Wang, E.-M. Shih, A. Ghiotto, L. Xian, D. A. Rhodes, C. Tan, M. Claassen, D. M. Kennes, Y. Bai, B. Kim, K. Watanabe, T. Taniguchi, X. Zhu, J. Hone, A. Rubio, A. N. Pasupathy, and C. R. Dean, Nat. Mater. **19**, 861 (2020).
[15] Z. Zhang, Y. Wang, K. Watanabe, T. Taniguchi, K. Ueno, E. Tutuc, and B. J. LeRoy, Nat. Phys. **16**, 1093 (2020).
[16] T. Li, S. Jiang, L. Li, Y. Zhang, K. Kang, J. Zhu, K. Watanabe, T. Taniguchi, D. Chowdhury, L. Fu, J. Shan, and K. F. Mak, Nature (London) **597**, 350 (2021).
[17] T. Li, S. Jiang, B. Shen, Y. Zhang, L. Li, T. Devakul, K. Watanabe, T. Taniguchi, L. Fu, J. Shan, and K. F. Mak, Nature (London) **600**, 641 (2021).
[18] J. Zang, J. Wang, J. Cano, and A. J. Millis, Phys. Rev. B **104**, 075150 (2021).
[19] F. Wu, T. Lovorn, E. Tutuc, and A. H. MacDonald, Phys. Rev. Lett. **121**, 026402 (2018).
[20] F. Wu, T. Lovorn, E. Tutuc, I. Martin, and A. H. MacDonald, Phys. Rev. Lett. **122**, 086402 (2019).
[21] C. Schrade and L. Fu, Phys. Rev. B **100**, 035413 (2019).
[22] H. Pan, F. Wu, and S. Das Sarma, Phys. Rev. Res. **2**, 033087 (2020).
[23] H. Pan, F. Wu, and S. Das Sarma, Phys. Rev. B **102**, 201104(R) (2020).
[24] Y. Zhang, N. F. Q. Yuan, and L. Fu, Phys. Rev. B **102**, 201115(R) (2020).
[25] Y. Zhang, T. Liu, and L. Fu, Phys. Rev. B **103**, 155142 (2021).
[26] T. Devakul, V. Crépel, Y. Zhang, and L. Fu, Nat. Commun. **12**, 6730 (2021).
[27] Y. Zhang, T. Devakul, and L. Fu, Proc. Natl. Acad. Sci. USA **118**, e2112673118 (2021).
[28] Y.-T. Hsu, F. Wu, and S. Das Sarma, Phys. Rev. B **104**, 195134 (2021).
[29] Z. Bi and L. Fu, Nat. Commun. **12**, 642 (2021).
[30] Y. Cao, V. Fatemi, S. Fang, K. Watanabe, T. Taniguchi, E. Kaxiras, and P. Jarillo-Herrero, Nature (London) **556**, 43 (2018).
[31] M. Yankowitz, S. Chen, H. Polshyn, Y. Zhang, K. Watanabe, T. Taniguchi, D. Graf, A. F. Young, and C. R. Dean, Science **363**, 1059 (2019).
[32] G. Chen, A. L. Sharpe, P. Gallagher, I. T. Rosen, E. J. Fox, L. Jiang, B. Lyu, H. Li, K. Watanabe, T. Taniguchi, J. Jung, Z. Shi, D. Goldhaber-Gordon, Y. Zhang, and F. Wang, Nature (London) **572**, 215 (2019).
[33] X. Liu, Z. Hao, E. Khalaf, J. Y. Lee, K. Watanabe, T. Taniguchi, A. Vishwanath, and P. Kim, Nature (London) **583**, 221 (2020).
[34] J. M. Park, Y. Cao, K. Watanabe, T. Taniguchi, and P. Jarillo-Herrero, Nature (London) **590**, 249 (2021).
[35] Z. Hao, A. Zimmerman, P. Ledwith, E. Khalaf, D. H. Najafabadi, K. Watanabe, T. Taniguchi, A. Vishwanath, and P. Kim, Science **371**, 1133 (2021).
[36] Y. Cao, J. M. Park, K. Watanabe, T. Taniguchi, and P. Jarillo-Herrero, Nature (London) **595**, 526 (2021).
[37] S. Raghu, S. A. Kivelson, and D. J. Scalapino, Phys. Rev. B **81**, 224505 (2010).

[38] W. Kohn and J. M. Luttinger, Phys. Rev. Lett. **15**, 524 (1965).
[39] A. V. Chubukov, Phys. Rev. B **48**, 1097 (1993).
[40] S. Maiti and A. V. Chubukov, AIP Conf. Proc. **1550**, 3 (2013).
[41] Y.-P. Lin and R. M. Nandkishore, Phys. Rev. B **98**, 214521 (2018).
[42] J. González and T. Stauber, Phys. Rev. Lett. **122**, 026801 (2019).
[43] A. Ghazaryan, T. Holder, M. Serbyn, and E. Berg, Phys. Rev. Lett. **127**, 247001 (2021).
[44] Y.-Z. You and A. Vishwanath, Phys. Rev. B **105**, 134524 (2022).
[45] T. Cea, P. A. Pantaleón, V. T. Phong, and F. Guinea, Phys. Rev. B **105**, 075432 (2022).
[46] M. Sigrist, AIP Conf. Proc. **789**, 165 (2005).
[47] P. A. Frigeri, D. F. Agterberg, A. Koga, and M. Sigrist, Phys. Rev. Lett. **92**, 097001 (2004).
[48] P. A. Frigeri, D. F. Agterberg, and M. Sigrist, New J. Phys. **6**, 115 (2004).
[49] See Supplemental Material at http://link.aps.org/supplemental/10.1103/PhysRevB.110.035143 for details on the derivation of the interaction vertex, the self-consistency equation, and the Ginzburg-Landau free energy, as well as a discussion on an effective triangular-lattice Hubbard model, which includes Refs. [51,57–60].
[50] Y.-T. Hsu, A. Vaezi, M. H. Fischer, and E.-A. Kim, Nat. Commun. **8**, 14985 (2017).
[51] N. F. Q. Yuan, K. F. Mak, and K. T. Law, Phys. Rev. Lett. **113**, 097001 (2014).
[52] W. Cho, R. Thomale, S. Raghu, and S. A. Kivelson, Phys. Rev. B **88**, 064505 (2013).
[53] J. W. F. Venderbos, V. Kozii, and L. Fu, Phys. Rev. B **94**, 094522 (2016).
[54] Y. Cao, D. Rodan-Legrain, J. M. Park, F. N. Yuan, K. Watanabe, T. Taniguchi, R. M. Fernandes, L. Fu, and P. Jarillo-Herrero, Science **372**, 264 (2021).
[55] Y. Xia, Z. Han, K. Watanabe, T. Taniguchi, J. Shan, and K. F. Mak, arXiv:2405.14784.
[56] Y. Guo, J. Pack, J. Swann, L. Holtzman, M. Cothrine, K. Watanabe, T. Taniguchi, D. Mandrus, K. Barmak, J. Hone, A. J. Millis, A. N. Pasupathy, and C. R. Dean, arXiv:2406.03418.
[57] R. Shankar, Rev. Mod. Phys. **66**, 129 (1994).
[58] L. Wang and O. Vafek, Physica C: Supercond. Appl. **497**, 6 (2014).
[59] C. Platt, W. Hanke, and R. Thomale, Adv. Phys. **62**, 453 (2013).
[60] T. Fukui, Y. Hatsugai, and H. Suzuki, J. Phys. Soc. Jpn. **74**, 1674 (2005).

Correction: A typographical error in the reference number in the last sentence of the paragraph in the Note Added section has been fixed.